Testing quartz and feldspar luminescence dating to determine earthquake and tsunami recurrence in the area of the giant 1960 Chile earthquake

Dominik Brill [a],[*], Marco Cisternas [b]

[a] *Institute of Geography, University of Cologne, Germany*
[b] *Instituto de Geografía, Pontificia Universidad Católica de Valparaíso, Chile*

ABSTRACT

Coasts on active subduction zones are recurrently affected by great earthquakes and associated tsunamis. Deposits resulting from both tidal inundation after coseismic subsidence and from tsunamis can be radiocarbon dated to infer patterns of earthquake and tsunami recurrence. Yet, finding suitable plant material for radiocarbon dating is not always easy. Luminescence dating provides a more ubiquitously applicable approach, but in such settings remains challenging due to three main reasons: (i) The quartz and feldspar minerals formed on active subduction zones tend to show inadequate luminescence properties; (ii) tsunami deposits may be affected by incomplete resetting of luminescence signals; and (iii) the dosimetry in sequences of tsunami and tidal sand sheets intercalated in marsh soils is often complicated. To evaluate the impact of these factors on luminescence dating accuracy, we re-date previously historically-constrained and radiocarbon dated tsunami and post-earthquake tidal deposits marking some predecessors of the giant 1960 Chile earthquake.

While the impact of complex dosimetry on luminescence ages was negligible for both quartz and feldspar, the selection of an appropriate luminescence signal and aliquot size was crucial for generating robust chronologies. Due to unstable luminescence signals, quartz optically stimulated luminescence (OSL) ages and fading corrected infrared-stimulated (IR_{50}) feldspar ages significantly underestimate the control ages. Only post-infrared-infrared ($pIRIR_{150}$) signals of feldspar provide ages without any systematic age underestimation. Incomplete signal resetting was successfully addressed by using small aliquots in combination with the bootstrapped minimum age model. Remaining remnant ages of a few decades to a few centuries for the historical 1960 and 1575 tsunami sand sheets reflect a combination of laboratory residuals and incomplete signal resetting.

Our results show that low-temperature pIRIR dating of feldspar is a valuable tool for reconstructing late Holocene earthquake chronologies in regions where quartz is geologically young, volcanic in origin, and holds few transportation cycles, as it occurs in active subduction zones. Although relatively large residual doses introduce dating uncertainties for sediments younger than a few centuries, feldspar pIRIR dating appears to be a good alternative to radiocarbon dating. On the contrary, quartz OSL and feldspar infrared ages were associated with systematic age underestimation, making them problematic for obtaining adequate chronologies in this type of geologic setting.

1. Introduction

Great megathrust earthquakes and associated tsunamis pose a serious threat to coastal populations living on subduction zones as lately shown by the disastrous 2004 Sumatra–Andaman, 2010 Chile, and 2011 Japan events. Since great earthquakes are generally rare and recur irregularly, long-term recurrence series are required for a robust hazard assessment (Satake and Atwater, 2007). Beyond coverage by instrumental and historical records, earthquake and tsunami recurrence can

be inferred from coastal paleoseismology. It includes dating geological evidence of both coseismic subsidence, such as post-earthquake tidal deposits overlying soils (Atwater and Hemphill-Haley, 1997), and tsunamis, marked by tabular sand sheets intercalated in marsh soils (Bourgeois, 2009).

Yet, coastal paleoseismology faces the problem of finding adequate plant material for radiocarbon dating those deposits. At sandy coasts, where preserved plant material is scarce, shells might be a solution; however, local marine reservoirs of carbon must be previously known

and considered (Bourgeois, 2009). Alternatively, luminescence dating envisages as one of the most direct approaches for dating tidal (e.g. Madsen et al., 2005) and tsunami (e.g. Banerjee et al., 2001; Cunha et al., 2010; Brill et al., 2012a, b) deposits, as providing the timing of the sedimentation itself.

Most luminescence studies on Holocene sediments have preferred quartz as dosimeter, because its signals are typically easy to bleach and stable over the time of burial. However, tsunami-generating subduction zones often correspond to active orogeny, which drives the production

of poorly-sensitized, sedimentologically immature quartz (e.g. Chamberlain et al., in press) that is often unsuitable for luminescence dating (Steffen et al., 2009; del Rio et al., 2019). Feldspar, as alternative dosimeter, has successfully been used to date young sediments (e.g. Riedesel et al., 2018); however, its signal is less light sensitive and often suffers from a signal loss over time, known as anomalous fading (Spooner, 1994). Both properties make feldspar less suitable for dating Holocene sediments. Therefore, approaches to separate stable luminescence signal components in young quartz samples, as made for deposits
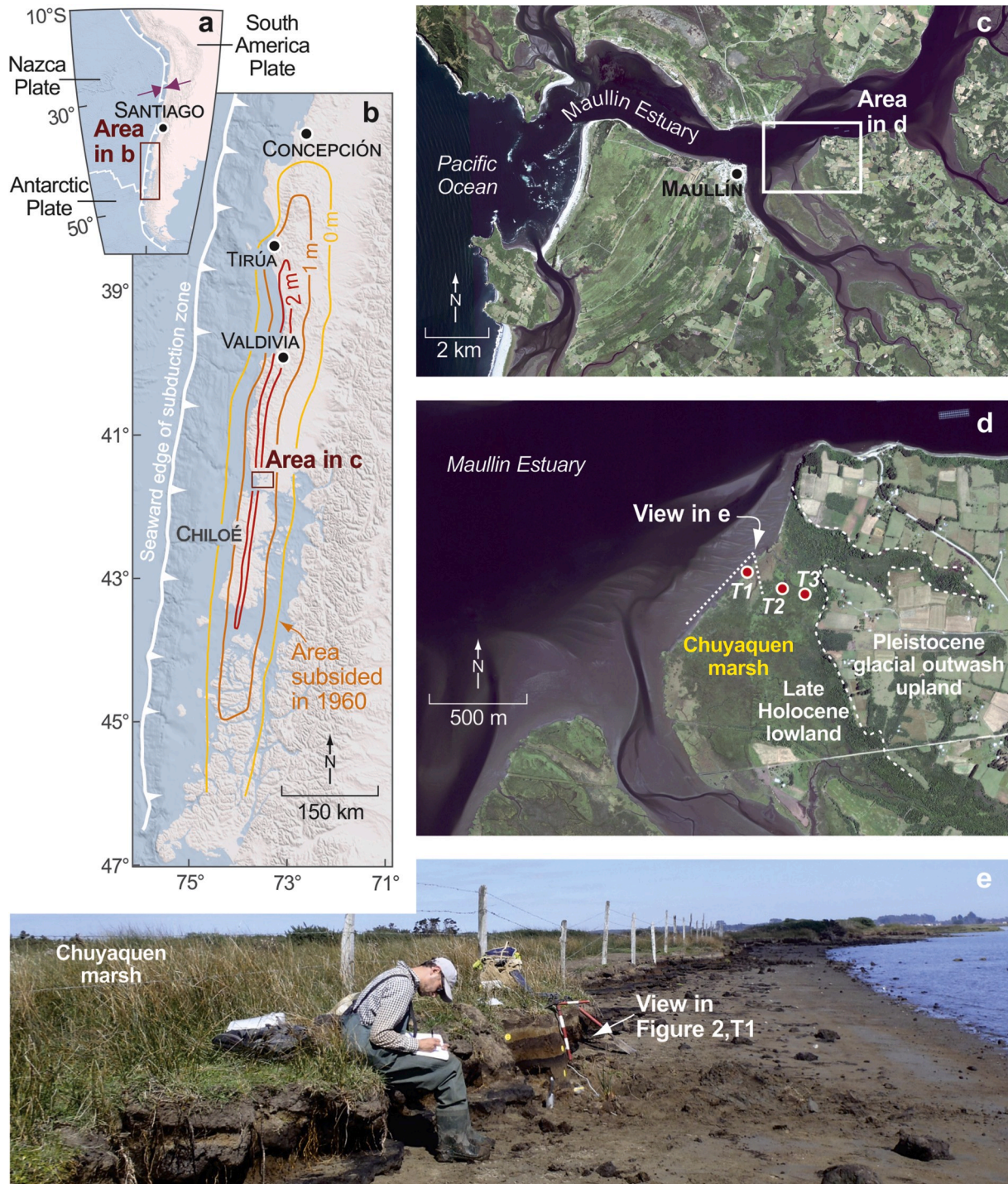

Fig. 1. Location and setting of the study site. a) Tectonic setting. b) Contour lines with an interval of 1 m showing the amount and area of subsidence associated to the giant 1960 Chile earthquake (Plafker and Savage, 1970). c) Maullin estuary (GoogleEarth©). d) Location and setting of the Chuyaquen marsh and sampling sites (T1, T2, T3; GoogleEarth©). e) Overview of the Chuyaquen marsh's coastline and location of the outcrop T1.

of the 869 Jōgan tsunami (Tamura et al., 2015), or techniques to extract well-bleached and stable potassium feldspar signals (Brill et al., 2018), are crucial for successful dating.

To gain further insight into the ability of the luminescence technique to date both Holocene post-subsidence tidal and tsunami deposits to determine earthquake and tsunami recurrence, we test quartz optically stimulated luminescence (OSL) and potassium feldspar infrared stimulated luminescence (IRSL) ages against control ages previously constrained from historical records and radiocarbon dating of plant material. Ages come from a stratigraphic sequence of sand sheets intercalated among marsh soils resulting from repetitive co-seismic subsidence and tsunami inundation in Chuyaquen, a saltmarsh located midway along the area that subsided during the giant 1960 Chile earthquake (Cisternas et al., 2005, Fig. 1). Comparing the results of different luminescence signals and different aliquot sizes with the control ages enabled us to study the combined effect of signal resetting and signal stability on quartz and potassium feldspar dating accuracy. As a further impact factor on the dating accuracy of coastal sediments, we analyzed the influence of heterogeneous radiation fields due to complex stratigraphy with episodic evolution. Additionally, we offer new radiocarbon ages for one earthquake and tsunami event that was not dated previously in Chuyaquen. With this addition, a two-millennia sequence of earthquakes and tsunamis in south central Chile is completed.

The good control ages for the sediments that we have re-dated with luminescence at Chuyaquen provide an exceptional opportunity for assessing the inaccuracies related to date tidal and tsunami deposits in seismically active settings. These insights, likely transferable to other coastal deposits in Chile and elsewhere, where young cordilleras exist, will help to improve long-term earthquake and tsunami hazard assessment on active subduction zones.

2. The earthquake and tsunami record at the Chuyaquen marsh, south central Chile

Chile, with one earthquake larger than M_w 8 every five to ten years (Barrientos, 2007), has one of the most seismically active coasts worldwide. Such activity results from the subduction of the Nazca plate beneath South America at rates of 6.6 cm/yr (Angermann et al., 1999, Fig. 1a). On May 22, 1960, an astonishing earthquake (M_w 9.5) broke the boundary between those plates (Cifuentes, 1989). The rupture extended along 1000 km of south central Chile, lowered one-quarter of the country's outer coast by ~1.5 m (Plafker and Savage, 1970, Fig. 1b) and likely changed Earth's rotational wobble (Kanamori and Cipar, 1974). Concurrent displacement of the seafloor generated a tsunami with peak heights of 15 m in Chile (Sievers, 1963), 10 m in Hawaii (Lander and Lockridge, 1989), and 6 m in Japan (Watanabe, 1998).

Three historical earthquakes of varying size, in 1575, 1737 and 1837, preceded the 1960 event (Lomnitz, 2004; Cisternas et al., 2005). While the spatial extent and severity of the effects in 1575 most closely resemble those in 1960, the 1737 and 1837 earthquakes seem smaller. The 1737 earthquake likely broke the northern half of the 1960 region, on a narrow and deep portion of the megathrust, whereas the 1837 rupture had broken the southern half, over a wide range of depth (Cisternas et al., 2017). A comparison of the spatial effects of the 1960 event and those of the 1575 event is shown in the supplementary material (Fig. S1).

Paleoseismological studies have extended this seismic history thousands of years into the past (Cisternas et al., 2005, 2018; Atwater et al., 2013; Ely et al., 2014; Moernaut et al., 2014, 2017; Garrett et al., 2015). Among these works, Cisternas et al. (2005) found at Chuyaquen, a marsh in the Maullín estuary midway along the 1960 rupture area, stratigraphic evidence of recurrent subsidence and tsunamis in the past 2000 years (Fig. 1a,b,c). This seismic chronology has been subsequently corroborated by regional evidence of: i) shaking-triggered turbidites in Andean lakes (Moernaut et al., 2014, 2018), ii) coastal landslides (Cisternas et al., 2018), iii) tsunami intrusions in a coastal lake (Kempf et al.,

2017), and iv) subsidence and tsunami inundation of shore lowlands (Atwater et al., 2013; Ely et al., 2014; Garrett et al., 2015).

The Chuyaquen evidence consists of eight nearly continuous, mostly tabular sand sheets, alternated with darker organic marsh soils, giving the stratigraphy a horizontally banded appearance (Fig. 2). Some of the sand sheets represent sandy tidal flats that record coseismic subsidence, while others record tsunami deposition. The sequence holds evidence of eight 1960-like earthquakes (events A-H). Events A and B represent the 1960 and 1575 historical earthquakes, respectively. The prehistoric events were radiocarbon dated by Cisternas et al. (2005), at 2 σ, to AD 1280–1390 (event C), AD 1020–1180 (event D), AD 441–654, (event F), and BC 18-AD 222 (event H). Although stratigraphically recognized, events E and G were not radiocarbon dated by Cisternas et al. (2005) due to lack of adequate plant material.

In this paper, we use and complement the Chuyaquen seismic sequence. On one hand, we use its chronology as control ages to test the ability of quartz OSL and potassium feldspar IRSL to date young post-subsidence tidal and tsunami deposits. On the other, we complement the Chuyaquen chronology offering: i) Luminescence ages for the previously undated event E; ii) Radiocarbon and luminescence ages for the previously undated event G; and iii) Luminescence ages to test against the ages of the previously radiocarbon dated events A, B, C, and D. Because neither we nor Cisternas et al. (2005) were able to find plant material to radiocarbon date event E at Chuyaquen, we will compare its new luminescence age with its radiocarbon age previously obtained from lacustrine turbidites (AD 668–773; Moernaut et al., 2017).

3. Material and methods

3.1. Sampling

We retraced the Chuyaquen stratigraphy along the main transect of Cisternas et al. (2005; Fig. 1d). During low tide, we cleaned the wall of a natural outcrop on the marsh's shore (T1; Fig. 1e) and dug two trenches inland at higher levels along the transect (T2, T3; Fig. 1d). We used the criteria of Cisternas et al. (2005), based on the modern analogs of the 1960 event, to differentiate between tidal and tsunami deposits. Diagnostic features include the characteristics of both the sand layers and the contacts between sand and the soils it buried. While tsunami deposits are tabular, <10 cm thick, and thicker only in depressions of the original surface, the thickness of the tidal sand is more variable, ranging between 5 and 60 cm, regardless of the original surface. The soil-sand contacts of tsunami deposits are abrupt, sharp, and continuous for meters, while the contact of tidal sand is riddled with burrows, up to 2 cm wide, dug by intertidal worms and crabs. Grain size of the sand is not diagnostic as being in all cases homogeneous, massive, fine to medium, well sorted sand. Once we identified and classified the seven sand sheets, according to their diagnostic features, we started sampling in the three stratigraphic columns.

For luminescence dating we sampled a total of seven sand sheets representing event A (MAU-A), event B (MAU-B), event C (MAU-C_1 and MAU-C_2), event D (MAU-D), event E (MAU-E), and event G (MAU-G; Fig. 2; Table 1). While sand sheets A, B, C_2 and D represent tsunami deposits, sand sheets C_1, E and G were identified as tidal deposits formed after coseismic subsidence. We could not find sand sheets representing events F and H thick enough to be adequately sampled. Luminescence samples were obtained from the cleaned and straighten walls of the outcrop and trenches. Steel tubes were horizontally thrust into the sand sheets and appropriately capped before extraction. Extra samples from each sand sheet and surrounding soils (S1 to S8) were obtained and stored in plastic bags to determine dose rates (Fig. 2). Finally, for radiocarbon dating of event G we used well preserved culms (buried stems) of the marsh rush *Juncus balticus. They were* found in growth position in the soil buried by the tidal-flat sand sheet deposited after coseismic subsidence of event G. Remains of *J. balticus* are used in paleoseismology because its culms and rhizomes grow horizontally
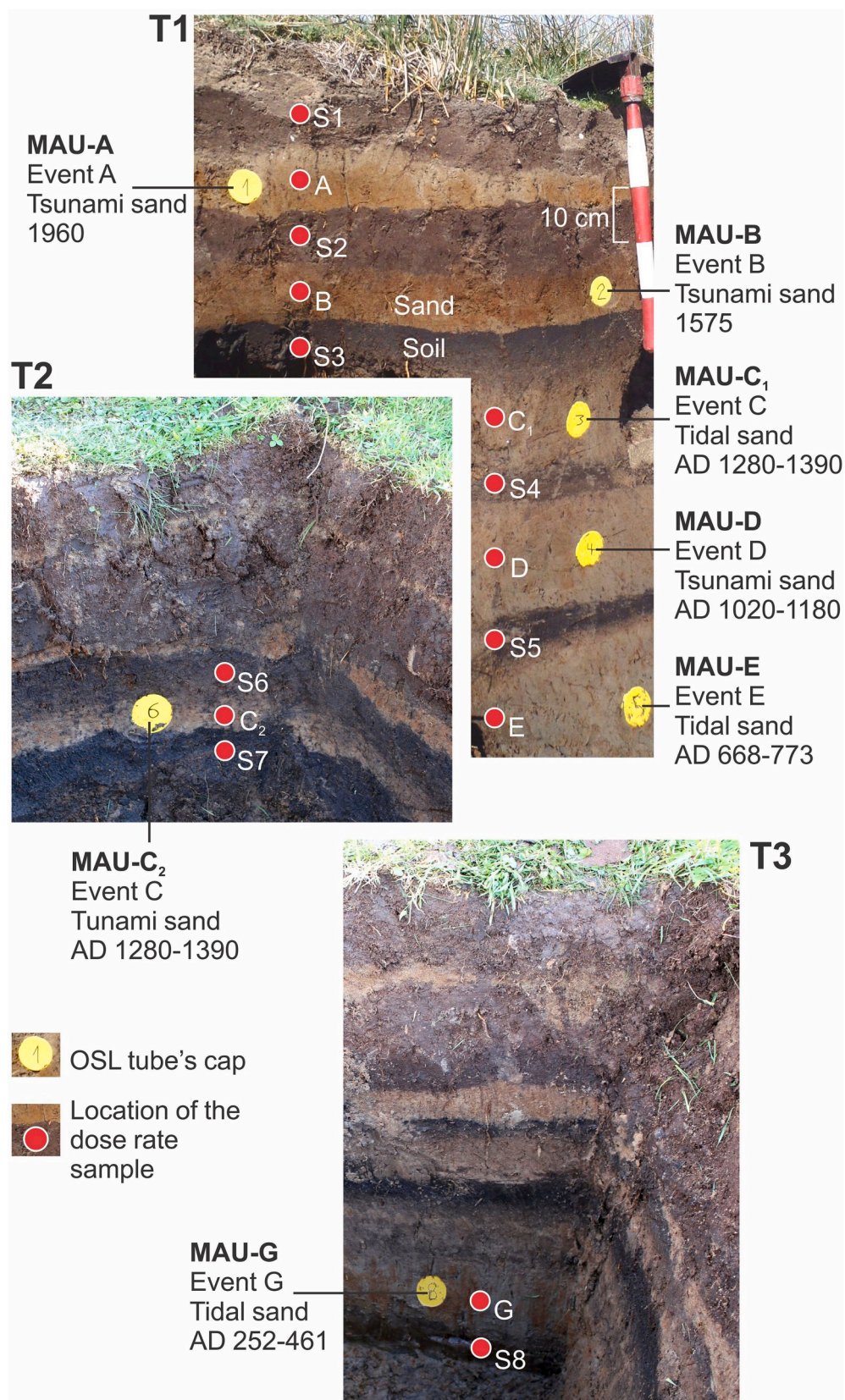
Fig. 2. Stratigraphy of Chuyaquen marsh and sampling locations. Sequences of marsh soils and sand sheets in the coastline outcrop (T1), and in inland trenches (T2, T3). Yellow circles are the plastic caps of the thrusted OSL tubes. Red labelled dots show the locations where the dose rate samples were taken and their respective assigned name.

Table 1
Compilation of dated sand sheets with their historical and radiocarbon control ages, as well as pIRIR$_{150}$ ages from this study.

Sample	Trench	Event	Historic event (years AD)	Interpretation	Inferred age by ^{14}C dating (years AD)	pIRIR$_{150}$ age (years AD)
MAU-A	T1	A	1960	Tsunami sand		1757 ± 82
MAU-B	T1	B	1575	Tsunami sand	1450–1616	1251 ± 190
MAU-C$_1$	T1	C		Tidal sand	1280–1390	1392 ± 89
MAU-D	T1	D		Tsunami sand	1020–1180	1054 ± 99
MAU-E	T1	E		Tidal sand	668–773	1140 ± 155
MAU-C$_2$	T2	C		Tsunami sand	1280–1390	1087 ± 83
MAU-G	T3	G		Tidal sand	252–461	39 ± 150

instead of vertically as most plants do. This rush was used previously for radiocarbon dating in Chuyaquen itself by Cisternas et al. (2005) and in the Pacific northwest of the United States (Atwater and Hemphill-Haley, 1997; Sherrod, 2001).

3.2. Laboratory

Since luminescence dating relies on the time dependent accumulation of latent energy in quartz and feldspar minerals due to ionizing radiation, and the resetting of this energy due to sunlight exposure, sediment ages are inferred by measuring the energy dose accumulated since the last sunlight exposure (burial dose) and the ionizing radiation received by the sediment per unit of time (dose rate).

In this study, dose rates were obtained from radionuclide concentrations of uranium (^{238}U), thorium (^{232}Th) and potassium (^{4}K) determined with high-resolution gamma spectrometry (Ortec HPGe gamma-ray detector) at the Cologne Luminescence Laboratory (CLL). Based on radionuclide concentrations and in-situ water contents, infinite-matrix dose rates were derived using the DRAC software (Durcan et al., 2015). To account for the effect of spatially variable radionuclide concentrations and water contents between sand sheets and soils on the gamma dose rates, the *scale_GammaDose* function implemented in the R-package "Luminescence" v. 0.9.0 (Riedesel et al., 2019) was applied. The function calculates the gamma dose rate at the sample position by scaling user inputs of uranium, thorium, potassium, sediment density, water content and thicknesses of all surrounding stratigraphic layers following Aitken (1985, appendix H). The reduced efficiency of alpha particles in generating feldspar luminescence signals was corrected using a-values of 0.07 ± 0.02 (infrared signal at 50 °C; IR$_{50}$) and 0.11 ± 0.02 (post-infrared-infrared signal, pIRIR) adopted from Kreutzer et al. (2014). The internal dose rate of potassium feldspar grains is based on empirical values of 12.5 ± 0.5% for their potassium concentration (Huntley and Baril, 1997).

Samples for burial dose determination were sieved to 100–150 μm, treated with HCl (10%), H$_2$O$_2$ (10%) and sodium oxalate to remove carbonates, organic matter and clay. Density liquid was used to separate quartz (2.62<quartz<2.68 g/cm^3) and potassium feldspar grains (<2.58 g/cm^3). A final HF etching (40%) for 40 min removed feldspar contamination and the alpha-radiation affected rim of the quartz grains. For luminescence measurements, quartz and feldspar grains were fixed on multi-grain aliquots with 1 mm (~50 grains) and 8 mm diameter (~3000 grains) using silicon spray, or on single-grain discs with hole diameters of 200 μm. All samples were measured on automated Risø TL/OSL readers with ^{90}Sr/^{90}Y beta sources delivering ~0.075 Gy/s at the sample position. Quartz signals were stimulated with blue LEDs centered at 470 nm and detected through Hoya U340 filters. Feldspar signals were stimulated with infrared LEDs centered at 870 ± 40 nm (multi-grain aliquots) or an infrared laser focused at 830 nm (single grains) and detected trough an interference filter with peak transmission at 410 nm.

Equivalent dose (D$_e$) measurements on quartz followed a standard SAR protocol (Murray and Wintle, 2003, Table 2a). The suitability of the selected quartz SAR protocol was verified by preheat-plateau experiments, dose-recovery tests with laboratory doses of ~4 Gy applied after signal resetting with blue LEDs at room temperature, and component fitting of continuous wave (CW) OSL signal curves. A pulse annealing

Table 2
Measurement protocols for quartz (a) and feldspar (b) applied in this study.

a) Quartz SAR protocol			b) pIRIR$_{150}$ protocol for potassium feldspar		
Step	Treatment	Signal	Step	Treatment	Signal
1	Preheat (180 °C for 10 s)		1	Preheat (180 °C for 60 s)	
2	Blue LEDs (40 s @ 125 °C)	Lx (OSL)	2	IR LEDs (200 s @ 50 °C) for SA	Lx (IR$_{50}$)
3	Test dose			IR laser (1.65 s @ 50 °C) for SG	
4	Cutheat (160 °C)		3	IR LEDs (200 s @ 150 °C) for SA	Lx (pIRIR$_{150}$)
5	Blue LEDs (40 s @ 125 °C)	Tx (OSL)		IR laser (1.65 s @ 150 °C) for SG	
6	Dose (R1-R4, R0, RR, DR)		4	Test dose	
7	Return to step 1		5	Preheat (180 °C for 60 s)	
			6	IR LEDs (200 s @ 50 °C) for SA IR laser (1.65 s @ 50 °C) for SG	Tx (IR$_{50}$)
R1-x = regeneration doses			7	IR LEDs (200 s @ 150 °C) for SA IR laser (1.65 s @ 150 °C) for SG	Tx (pIRIR$_{150}$)
RR = recycling dose, DR = depletion ratio			8	IR LEDs (100 s @ 200 °C)	
R0 = zero dose (recuperation)			9	Dose (R1-R4, R0, RR)	
SG = single grain, SA = single aliquot			10	Return to step 1	

experiment with temperatures between 200 and 400 °C (raised in steps of 20 °C) was performed to check for signal stability (cf. Fan et al., 2011). Potassium feldspar extracts were measured using a pIRIR protocol (Thomsen et al., 2008) with a low post infrared stimulation temperature of 150 °C (pIRIR$_{150}$; e.g. Madsen et al., 2011 and Reimann and Tsukamoto, 2012) (Table 2b). Low-temperature pIRIR protocols allow for successively measuring two signals for dating, the signal of the first-IR stimulation at 50 °C (IR$_{50}$) and the pIRIR signal measured at elevated temperature (here pIRIR$_{150}$). While IR$_{50}$ signals usually bleach more rapidly but are affected by significant fading, low-temperature pIRIR signals offer a compromise between signal stability (i.e. no or insignificant fading) and signal resetting (i.e. remnant doses as low as <0.2 Gy for the best-bleached grains; Reimann and Tsukamoto, 2012; Brill et al., 2018). The selection and performance of the pIRIR$_{150}$ protocol for the samples of this study were evaluated by means of dose-recovery tests and residual doses remaining after 24 h of solar simulator bleaching. In addition, fading experiments with delay times between dosing and measurement of up to ~48 h were performed.

While a standard late background subtraction was applied to derive feldspar D$_e$s, quartz equivalent doses were based on early background subtraction (Cunningham and Wallinga, 2010) to increase the contribution of the fast component. In the best case, this can help to reduce the potential effects of incomplete signal resetting or unstable signal components. All aliquots that passed the SAR acceptance criteria in terms of recycling ratio (0.9–1.1), recuperation (5% of larges regenerative dose)

and, in case of quartz measurements, depletion ratio (0.9–1.1) were considered for burial dose calculation. Burial doses for all samples and signals were based on the minimum age model (Galbraith et al., 1999) combined with a bootstrapping approach (MAM$_{bs}$; Cunningham and Wallinga, 2012). The fading correction for feldspar ages was conducted using the approach of Huntley and Lamothe (2001).

Accelerator mass spectrometry (AMS) radiocarbon analysis provided ages for two *Juncus balticus* culms buried by the tidal sand sheet marking event G (Table 3). Samples were carefully cleaned under the microscope to extract modern rootlets and sent to Beta Analytic Laboratory. The obtained radiocarbon ages were calibrated to years AD and BP at 2 σ. For calibration we used the Southern Hemisphere data set of Hogg et al. (2013) and the software Calib Rev 7.0.4 (http://www.calib.qub.ac.uk/calib/).

4. Results and interpretation

4.1. Radiocarbon age of event G

Two *Juncus balticus* culms buried by the tidal sand sheet marking event G date this earthquake to AD 229–407 (Beta-217015) and AD 375–570 (Beta-217016). Their pooled mean age, 1705 ± 28 ^{14}C cal. yr BP, corresponds to AD 252–461. This date is stratigraphically consistent with both the age of the preceding event H (BC 18-AD 222), and that of the following event F (AD 441–654), recorded by the under- and overlying sand sheets, respectively.

4.2. The dosimetry of the Chuyaquen sedimentary record

Significant vertical variations of radionuclide concentrations and water contents were observed in all three studied stratigraphic columns (T1-T3), particularly between sand sheets and intervening organic soils (Fig. 3; Table S1). Sand sheets are characterized by radionuclide contents that exceeded those of the surrounding soils by 19% for uranium, 8% for thorium, and 25% for potassium on average. On the contrary, water contents in the sand sheets are on average 75% lower than in the soils. Consequently, infinite-matrix dose rates of sand sheets, calculated by DRAC, are significantly larger than those of the constraining soils (Fig. 3). While gamma dose rates show an average difference of 84%, total infinite-matrix dose rates vary by 39% for feldspar and 66% for quartz. The smaller effect on feldspar is due to the internal dose rates of ~0.54 Gy/ka, which is not affected by spatial inhomogeneity and accounts for 30% and 40% of the total infinite matrix dose rates of sand sheets and soils, respectively.

Since sand sheets, around 10 cm thick, receive gamma radiation from a sphere of approximately 30 cm in diameter, the dose rate at the sampling position is influenced by the gamma radiation of under- and overlying strata. Layer-specific gamma dose rates account for the gamma ray contribution of surrounding strata as a function of layer density and distance from the sample. These dose rates show significantly smaller spatial variability than infinite matrix dose rates (Fig. 3), and would reflect much better the real radiation the sand sheets have been exposed to.

Gamma and cosmic dose rates also varied with time in all studied sediment sections. Sediment overburden increased episodically shortly after the occurrence of the recorded events, including the deposits marking subsidence and tsunami inundation. To quantify the effect of successively increasing sediment thickness, individual dose rates for each depositional phase were calculated. While external gamma dose

rates tend to increase with additional sediment cover, the associated cosmic dose rates decline. These combined effects led to a small impact on environmental dose rates (Fig. 4). By using the temporally resolved dose rates and the control ages to calculate burial doses accumulated between the deposition of successive sand layers, quartz and feldspar luminescence ages were accordingly corrected. The overall impact of temporal dose rate variability on the luminescence ages did not exceed 5% (Fig. 4). The spatial heterogeneities of gamma dose rates described in the previous paragraph introduce dating errors by on average less than 4% for quartz and 3% for potassium feldspar (Fig. 3). However, to avoid biasing of the luminescence ages, the dose rates that consider both spatial and temporal variability of gamma and cosmic radiation are used for all further age calculations.

Another potential source of erroneous luminescence ages in low coastal settings, with high water tables and sediments rich in marine carbonates, are time-variable dose rates due to radioactive disequilibria in the ^{232}Th and ^{238}U decay chains (Olley et al., 1996; Zander et al., 2007). Disequilibria may result from both initial uranium or thorium uptake during carbonate formation (i.e. closed systems) or water-influenced mobility of radioactive nuclides in soluble carbonates (i.e. open systems). For the Chuyaquen sand sheets, gamma spectrometry indicates that activities of daughter isotopes in the ^{232}Th and ^{238}U decay chains vary on average by 21% and 26%, respectively (Table S2). Maximum variabilities of decay rates reach 31% for thorium and 42% for uranium. As postulated by Olley et al. (1996), disequilibria of up to 50% are quite common for coastal deposits. Such values have little effect however, less than 3%, on the final luminescence ages for closed systems. Based on the lack of a clear vertical trend in radionuclide concentrations, common in open systems, we infer the Chuyaquen sequence behaves as a closed system (Fig. 3a). Thus, we considered the U and Th disequilibria had little effect on the Chuyaquen luminescence ages, and accordingly they were not corrected.

4.3. Quartz OSL dating

4.3.1. Quartz luminescence properties

Quartz OSL properties were checked through standard experiments. Preheat-plateau tests show independence of thermal treatment only for low preheat temperatures between 140 and 200 °C (Fig. 5a). Higher temperatures result in large recuperation and a poor recovery of laboratory doses. However, with the selected preheat temperature of 180 °C, acceptable dose recovery tests were achieved for all samples (dose recovery ratios of 0.90–0.98; Fig. S2a) while recuperation and thermal transfer (both ~0.1 Gy) are still significant compared to the low natural doses of the samples. Fitting of natural and regenerative CW-signal curves (using laboratory doses of up to 50 Gy) indicated only moderate contributions of the quartz fast component (Fig. S2, Fig. S3b), which is typically stable and easy to bleach. Even with early-background subtraction the fast component accounted for only 40–50% of both natural and regenerated OSL signals. This did also not change with additional sensitization during repeated dosing and bleaching in the laboratory (Fig. S3c). Although D$_e$(time) plots do not offer clear evidence of unstable net quartz OSL signals (i.e. the dose is not falling with increasing length of the signal integral, Fig. 5e), pulse annealing experiments point to net OSL signals that are thermally unstable already at temperatures of 180–200 °C (Fig. 5d).

Seven quartz samples were tested. Large aliquots (8 mm, ~3000 grains) were measured, because low OSL intensities prevented using smaller aliquots or even single grains. The corresponding D$_e$

Table 3

Radiocarbon ages of two culms of *J. balticus* found in live position in the soil buried by sand sheet G.

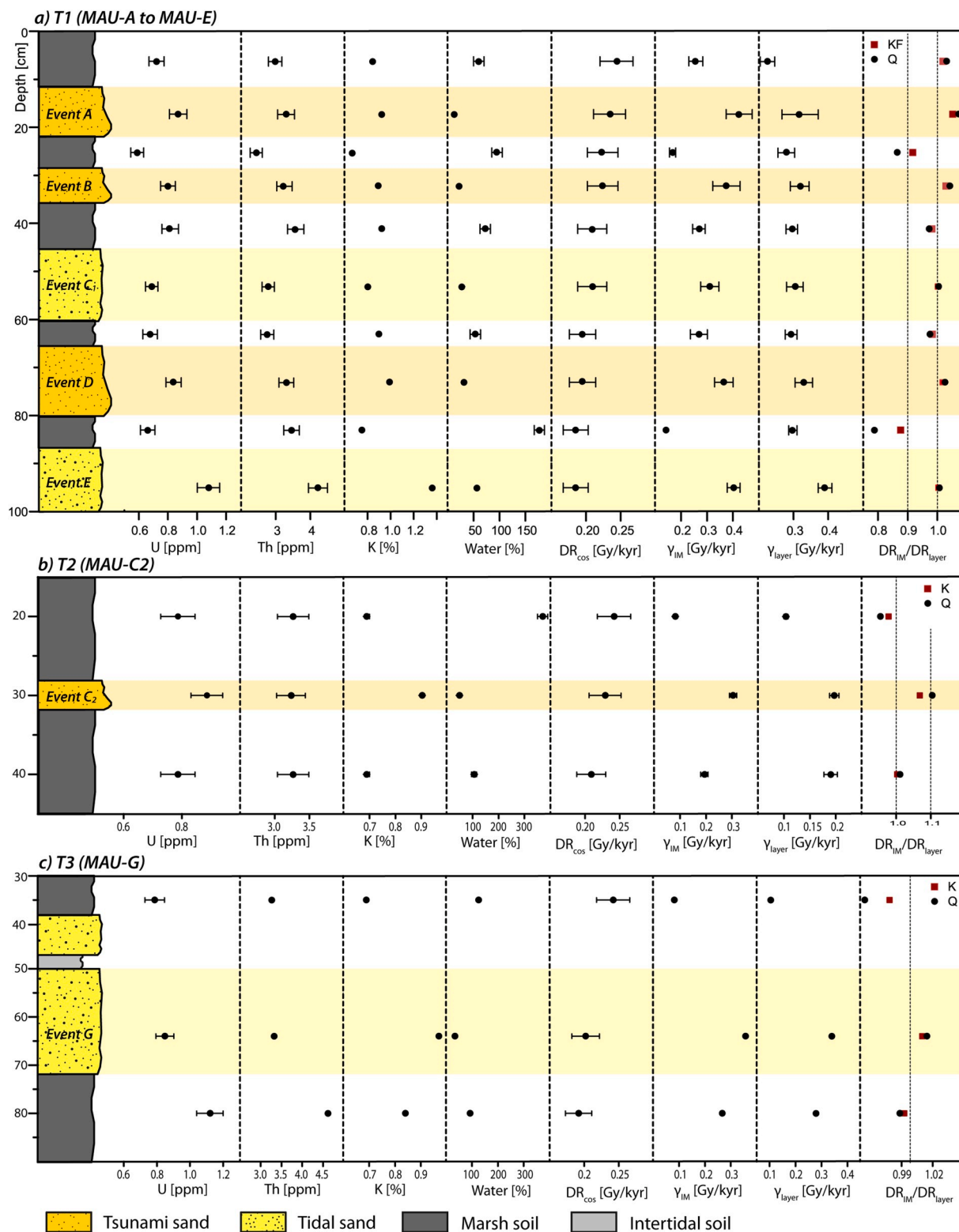| Lab-ID	Material	^{13}C/^{12}C ratio	Conventional radiocarbon age (yr BP)	Calibrated age(yr AD)
Beta-217015	*J. balticus* culm	−26.1°/oo	1770 ± 40	229–407
Beta-217016	*J. balticus* culm	−24.1°/oo	1640 ± 40	375–570

Fig. 3. Vertical variability of radionuclide concentrations (U, Th, K), water contents and dose rates in the stratigraphy of the coastline outcrop T1 (a), and inland trenches T2 (b) and T3 (c). DR$_{cos}$ – cosmic dose rate, γ_{IM} – infinite matrix gamma dose rate, γ_{layer} – layer-specific gamma dose rate, DR$_{IM}$/DR$_{layer}$ – ratio between total infinite matrix dose rate and total layer specific dose rate.

distributions were characterized by small to moderate scatter with over-dispersion values (obtained with the central age model, CAM cf. Galbraith et al., 1999) between 16 and 67% (see MAU-A and MAU-D in Fig. 6 for exemplary samples with large and small over-dispersion; the D$_e$ distributions of all other samples are shown in Fig. S4). Combined with the right skewedness of the dose distribution, at least for the youngest sand sheet (MAU-A), incomplete signal resetting is indicated and thus the bootstrapped minimum age model (MAM$_{bs}$) was applied for burial dose calculation. Based on the lowest over-dispersion of the seven samples, the expected over-dispersion of a well-bleached sample from
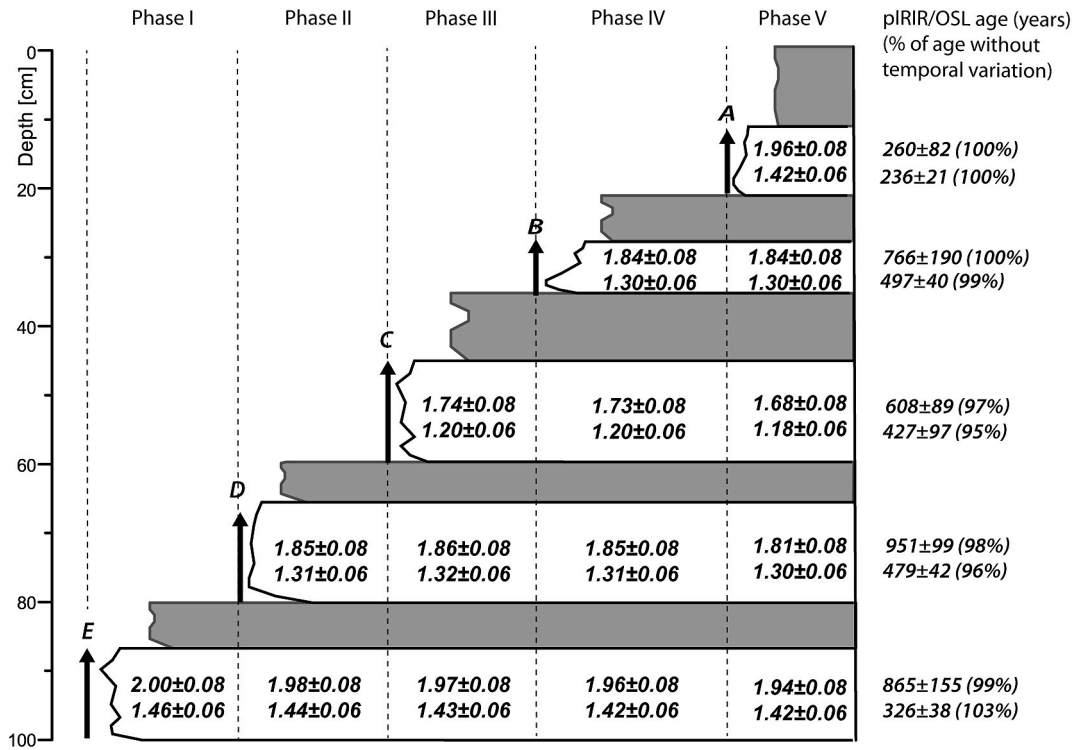
Fig. 4. Temporal variations of dose rates due to changing sediment overburden with time. The values in the deposits indicate environmental dose rates for feldspar (upper values) and quartz (lower values).

this setting (σ_b) was estimated to 15 ± 10%. For the older deposits, convergence of MAM_{bs} and the CAM points to more homogeneous signal resetting (see Table 4 for a summary of the most important OSL data).

4.3.2. Test of quartz ages against age controls

The accuracy of quartz OSL ages, which considered the MAM_{bs} for burial dose determination and the layer-specific gamma dose contributions for dose rate calculation, was evaluated against the historical and radiocarbon age controls (Table 1; Fig. 7a). Most quartz ages underestimate significantly the control ages, except for the ages of the younger, historical events of 1960 and 1575 (MAU-A and MAU-B), which were overestimated by 180 ± 20 and 60 ± 35 years, respectively. Despite such overestimation, the latter age falls within the 1-σ dating uncertainty. Conversely, the quartz ages of all older samples, either tsunami or tidal deposit, underestimate their control age by few centuries (230 ± 160 years for MAU-C_1) to over a millennium (1340 ± 150 years for MAU-G). Two main trends can be drawn from this comparison. First, quartz underestimation of the control ages increases with the deposit age, and second, the degree of underestimation does not appear linked to the kind of deposit, with no systematic difference between tsunami and tidal sediments.

4.4. Feldspar dating

4.4.1. Feldspar luminescence properties

Potassium feldspar was dated using the $pIRIR_{150}$ protocol. Experiments with stepwise increasing pIRIR and preheat temperatures (preheat is always 20 °C above the respective pIRIR temperature) show that the residual doses increase from <0.1 Gy at 110 °C to nearly 10 Gy at 290 °C in case of the pIRIR signal, and from <0.1 Gy to nearly 2 Gy in case of the associated IR_{50} signals (Fig. 5b). Dose recovery tests indicate adequate recovery of laboratory doses after residual subtraction for pIRIR temperatures between 110 and 180 °C for both the IR_{50} signal (0.91 ± 0.02 to 0.97 ± 0.03) and pIRIR signals (0.87 ± 0.04 to 1.04 ± 0.04). Finally, pIRIR signals measured at temperatures ≥150 °C are

characterized by g-values <2.0%/decade, while those of the IR_{50} signal remain relatively stable at 2.5–3.0%/decade (Fig. 5b). Thus, the selected $pIRIR_{150}$ protocol is a compromise between a stable pIRIR signal with low or insignificant fading (1.1–1.8%/decade) and relatively low laboratory residual doses of 0.28–0.65 Gy (Fig. 5c). The residual doses of the associated IR_{50} signal are lower at 0.10–0.23 Gy, while it reveals significant fading with g-values of 3.0–4.2%/decade (Fig. 5c). Residual doses still accounted for significant percentages of the natural doses of the sand sheets, i.e. 11–30% for IR_{50} and 8–42% for $pIRIR_{150}$, respectively, when excluding the youngest sample MAU-A for which residuals equaled 80–90% of the burial dose. We did not subtract these residual doses from the IR_{50} burial doses since these clearly underestimate the control ages (see section 4.4.2), but compared ages determined with and without residual subtraction for $pIRIR_{150}$.

Feldspar measurements were performed on small aliquots (1 mm) for all samples to allow for the detection and correction of incomplete bleaching. The corresponding IR_{50} D_e distributions are moderately scattered with over-dispersion values between 62% (MAU-A; Fig. 6b) and 15–23% (e.g. MAU-D in Fig. 6e; see Fig. S5 for the D_e distributions of all other samples). To address partial bleaching, burial dose calculation is based on the MAM_{bs} applied with a σ_b value of 15% and relatively large uncertainties of 10% (lowest over-dispersion of the sample set). The $pIRIR_{150}$ D_e distributions are slightly stronger scattered, with over-dispersion values between 61 and 70% (e.g. MAU-A; Fig. 6c) and 25–35% (e.g. MAU-D in Fig. 6f; see Fig. S6 for the D_e distributions of all other samples). While the MAM_{bs} is used for $pIRIR_{150}$ burial dose determination as well, it was applied with a slightly larger σ_b of 25 ± 10%. Finally, the IR_{50} ages were corrected for fading using the sample-specific g-values of 3.0–4.2%/decade (see Table 4). No correction was applied to the $pIRIR_{150}$ ages, since g-values of 1.1–1.8%/decade are interpreted to indicate insignificant fading (cf. Buylaert et al., 2012). The feldspar luminescence properties and ages of all seven samples are summarized in Table 4.
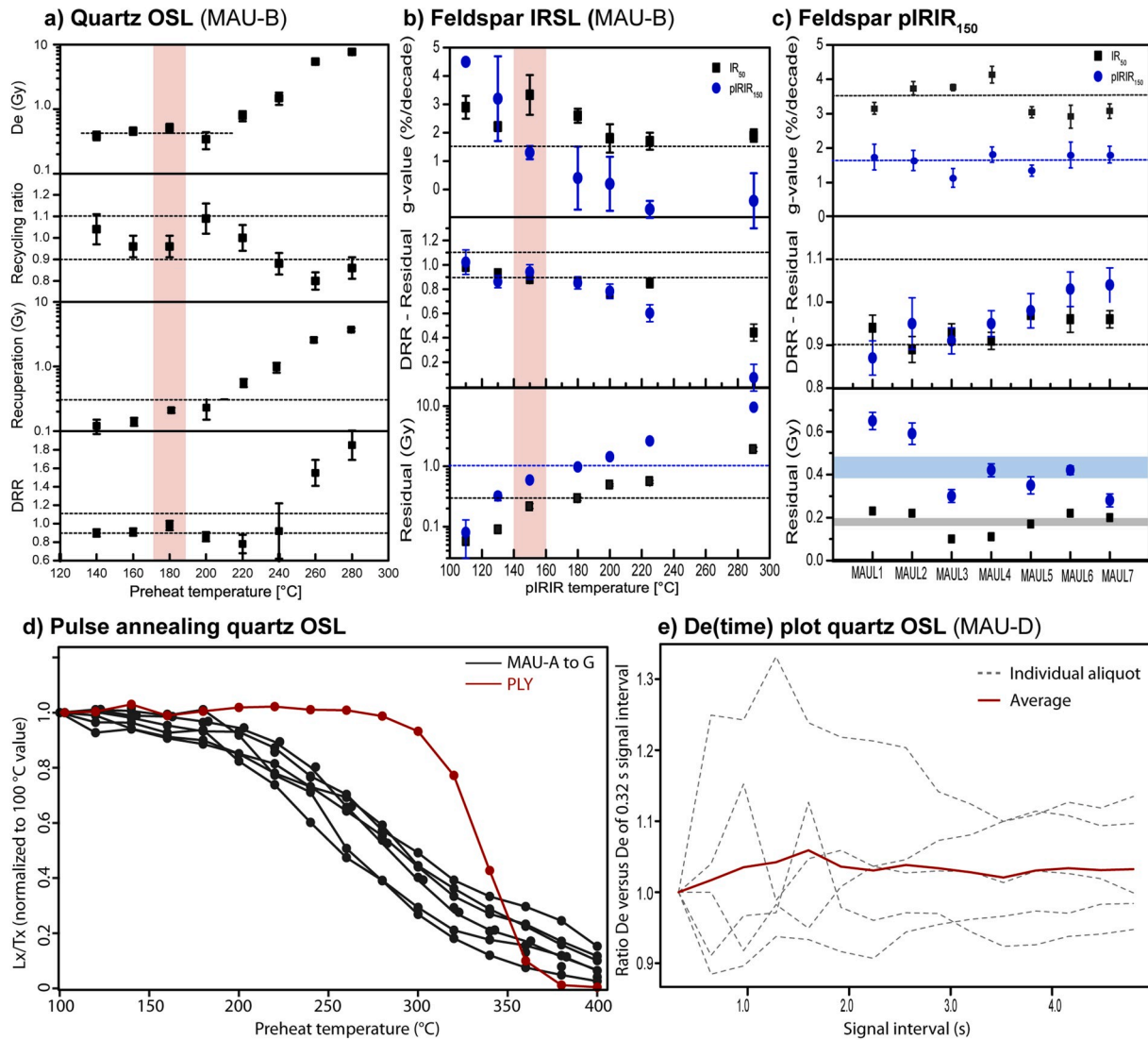
Fig. 5. Evaluation of quartz OSL and feldspar post-IRIR protocols. a) Quartz OSL preheat experiment performed on sample MAU-B. The preheat dependence was tested for natural doses (D_e) and recovered doses within a dose recovery test (DRT). b) Feldspar protocol evaluation by means of residual dose, dose recovery, and fading measurements with increasing pIRIR and preheat temperatures performed for sample MAU-B. The temperature combination of the selected protocol is shaded red. c) Determination of residual doses, recovery of laboratory doses and signal loss due to fading with the selected pIRIR$_{150}$ protocol for all seven samples. d) Pulse annealing experiment for the seven quartz samples from this study in comparison with an Australian quartz sample with perfect signal behavior (PLY 25-1, see Brill et al., 2017 for details about this sample). e) D_e(time) plots (i.e. De plotted against increasing signal integration intervals between 0.32 s and 4.8 s) for five aliquots of sample MAU-D.

4.4.2. Test of feldspar ages against control ages

The accuracy of feldspar ages, based on the MAM$_{bs}$ and layer-specific gamma dose rates, was also evaluated against the historical and radio-carbon independent age controls (Fig. 7b and c). IR$_{50}$ ages systematically underestimate the age control of most samples except those of the two younger ones, which areoverestimated, just as quartz does. However, the remnant IR$_{50}$ ages are much smaller than those obtained by quartz. IR$_{50}$ ages of the 1960 and the 1575 tsunami sand sheets (MAU-A and MAU-B) overestimate their control ages by 70 ± 10 and 160 ± 45 years, respectively, and underestimate the age of the five older ones ranging between 110 ± 100 and 490 ± 110 years (Fig. 7b). Even after fading correction, IR$_{50}$ ages show a tendency of increasing underestimation with deposition age and exhibit no systematic difference between tsunami and tidal sediments (Fig. 7b).

Tendencies of the pIRIR$_{150}$ ages without residual subtraction differ from those of quartz and IR$_{50}$. First, they do not underestimate the age of most samples but only one. Second, pIRIR$_{150}$ ages do not show the tendency of increasing underestimation with deposition age. Third, and most important, three out of seven pIRIR$_{150}$ ages (MAU-C1, MAU-D and MAU-G) overlap with their respective control ages within 1-σ dating uncertainties. Discrepancies with the control ages mainly arose from age overestimation of the younger samples; while residual dose subtraction eliminated overestimation of younger samples, it introduced a trend towards underestimation of the older ones (Fig. 7c). On the other hand, the pIRIR$_{150}$ ages do share with quartz and IR$_{50}$ ages the lack of a systematic difference between tsunami and tidal sediments (Fig. 7c).

To evaluate the influence of aliquot size on feldspar dating accuracy, large 8 mm-diameter aliquots (~3000 grains) and single grains were measured for the two younger samples (MAU-A and MAU-B) in addition to the 1 mm-diameter aliquots (~50 grains) measured previously (Fig. 8). Results for both samples show a trend towards decreasing remnant ages with decreasing aliquot size. This effect is particularly pronounced for the MAU-B sample, where single grain measurements reduce the multi-grain remnant ages from 320-850 to 40–420 years, for pIRIR$_{150}$, and from 160-270 to 0–50 years for IR$_{50}$ (Fig. 8b). Although single grains also reduce the IR$_{50}$ remnant ages of MAU-A, from 70-100
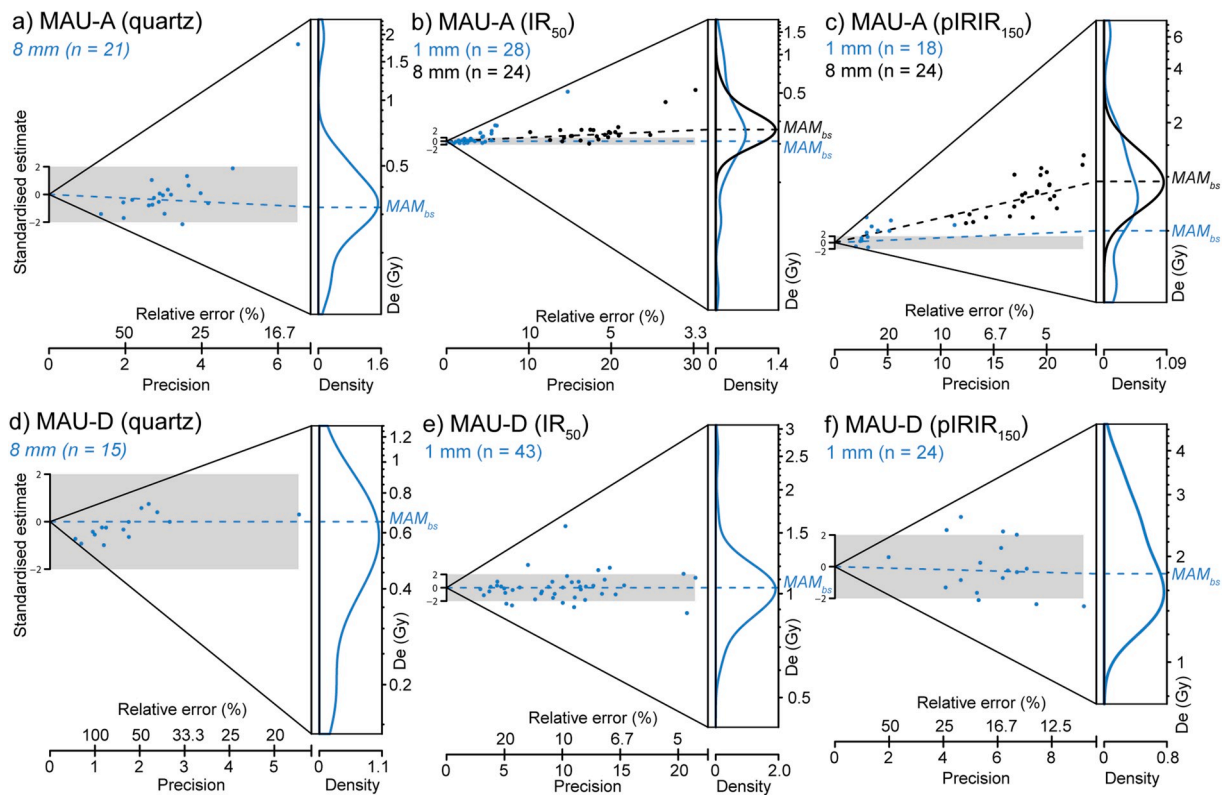
Fig. 6. Equivalent dose distributions for sand sheets of the 1960 tsunami (a–c) and a prehistoric tsunami in ~AD 1100 (d–f). All dose distributions of quartz (a, d), IR$_{50}$ (b, e) and pIRIR$_{150}$ signals (c, f) are shown as abanico plots.

Table 4
Summary of the most important information for burial dose determination for all dated samples. Size – aliquot size, N – number of accepted aliquots, OD – over-dispersion, σ_b – expected over-dispersion of a well bleached sample, MAM$_{bs}$ De – equivalent dose based on the bootstrap minimum age model, DR$_{layer}$ – layer-specific dose rate, Age$_{uncor}$ – uncorrected luminescence age, Age$_{cor}$ – fading corrected luminescence age, Ind. age – historical and radiocarbon age control.

Sample (ID)	Protocol	Size (mm)	N	OD (%)	σ_b (%)	MAM$_{bs}$ D$_e$ (Gy)	DR$_{layer}$ (Gy/kyr)	Age$_{uncor}$ (yrs)	g-value (%/dec)	Age$_{cor}$ (yrs)	Ind. age (yrs)
MAU-A	Q-SAR	8	21	48 ± 11	15 ± 10	0.34 ± 0.03	1.42 ± 0.09	**236 ± 21**	–	–	57
C-L4386	IR$_{50}$	SG	60	115 ± 24	15 ± 10	0.18 ± 0.03	1.96 ± 0.09	92 ± 15	3.2 ± 0.2	**114 ± 20**	
		1	28	62 ± 11		0.20 ± 0.02		102 ± 10		**127 ± 13**	
		8	24	24 ± 4		0.25 ± 0.02		128 ± 10		**159 ± 13**	
	pIRIR$_{150}$	SG	14	43 ± 19	25 ± 10	1.06 ± 0.26	1.96 ± 0.09	**542 ± 107**	1.8 ± 0.4	-	
		1	18	70 ± 15		0.51 ± 0.16		**260 ± 82**		–	
		8	24	24 ± 4		0.90 ± 0.09		**459 ± 46**		–	
MAU-B	Q-SAR	8	14	17 ± 5	15 ± 10	0.65 ± 0.05	1.30 ± 0.08	**500 ± 35**	–	–	442
C-L4387	IR$_{50}$	SG	57	79 ± 14	15 ± 10	0.54 ± 0.11	1.84 ± 0.08	313 ± 60	3.8 ± 0.2	**415 ± 80**	
		1	27	28 ± 5		0.83 ± 0.06		451 ± 33		**602 ± 46**	
		8	12	24 ± 5		0.98 ± 0.09		533 ± 49		**714 ± 69**	
	pIRIR$_{150}$	SG	14	93 ± 21	25 ± 10	1.24 ± 0.35	1.84 ± 0.08	**674 ± 190**	1.7 ± 0.3	-	
		1	23	61 ± 10		1.41 ± 0.35		**766 ± 190**		–	
		8	12	23 ± 5		2.39 ± 0.16		**1299 ± 87**		–	
MAU-C1	Q-SAR	8	14	31 ± 6	15 ± 10	0.51 ± 0.12	1.14 ± 0.08	**451 ± 105**	–	–	682 ± 55
C-L4388	IR$_{50}$	1	26	23 ± 5	15 ± 10	0.70 ± 0.08	1.68 ± 0.08	417 ± 48	3.8 ± 0.1	**556 ± 65**	
	pIRIR$_{150}$	1	19	35 ± 8	25 ± 10	1.05 ± 0.15	1.68 ± 0.08	**608 ± 89**	1.1 ± 0.3	–	
MAU-D	Q-SAR	8	15	16 ± 3	15 ± 10	0.63 ± 0.05	1.27 ± 0.08	**498 ± 36**	–	–	917 ± 80
C-L4389	IR$_{50}$	1	43	19 ± 3	15 ± 10	1.01 ± 0.05	1.81 ± 0.08	558 ± 28	4.2 ± 0.3	**773 ± 48**	
	pIRIR$_{150}$	1	24	26 ± 6	25 ± 10	1.76 ± 0.18	1.81 ± 0.08	**951 ± 99**	1.8 ± 0.2	–	
MAU-E	Q-SAR	8	25	26 ± 5	15 ± 10	0.44 ± 0.05	1.40 ± 0.08	**316 ± 35**	–	–	1297 ± 52
C-L4390	IR$_{50}$	1	41	19 ± 3	15 ± 10	1.23 ± 0.09	1.94 ± 0.08	634 ± 46	3.1 ± 0.2	**804 ± 61**	
	pIRIR$_{150}$	1	20	40 ± 8	25 ± 10	1.70 ± 0.30	1.94 ± 0.08	**865 ± 155**	1.4 ± 0.2	–	
MAU-C2	Q-SAR	8	22	67 ± 11	15 ± 10	0.21 ± 0.03	1.03 ± 0.10	**205 ± 29**	–	–	682 ± 55
C-L4391	IR$_{50}$	1	44	18 ± 2	15 ± 10	0.72 ± 0.05	1.57 ± 0.10	459 ± 32	3.0 ± 0.3	**575 ± 44**	
	pIRIR$_{150}$	1	23	32 ± 6	25 ± 10	1.46 ± 0.13	1.57 ± 0.10	**930 ± 83**	1.8 ± 0.4	–	
MAU-G	Q-SAR	8	19	36 ± 9	15 ± 10	0.40 ± 0.06	1.26 ± 0.10	**317 ± 48**	–	–	1660 ± 105
C-L4392	IR$_{50}$	1	36	15 ± 2	15 ± 10	1.66 ± 0.11	1.80 ± 0.10	922 ± 61	3.1 ± 0.2	**1180 ± 86**	
	pIRIR$_{150}$	1	20	25 ± 5	25 ± 10	3.56 ± 0.27	1.80 ± 0.10	**1978 ± 150**	1.8 ± 0.2	–	

Numbers shown in bold letters indicate the ages that are used for interpretation, i.e. fading corrected IR50 ages, and uncorrected quartz and pIRIR150 ages.
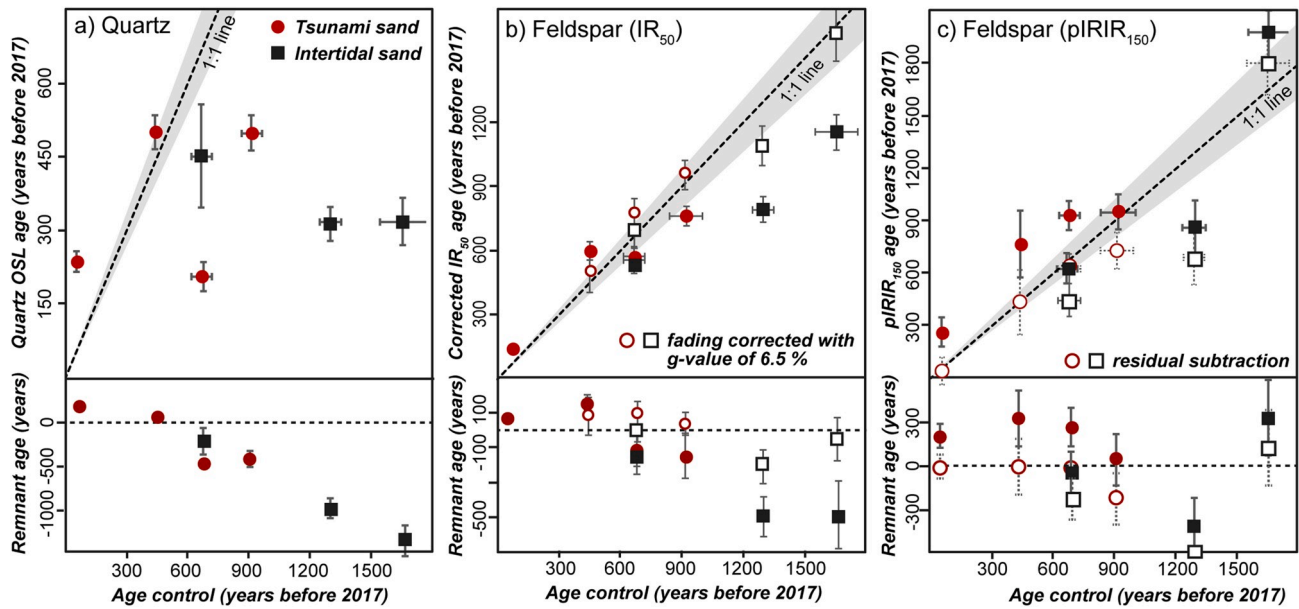
Fig. 7. Evaluation of OSL dating accuracy. The quartz (a), feldspar IR_{50} (b) and feldspar $pIRIR_{150}$ ages (c) of all samples (measured on 1 mm aliquots), as well as the corresponding remnant ages plotted against control ages.
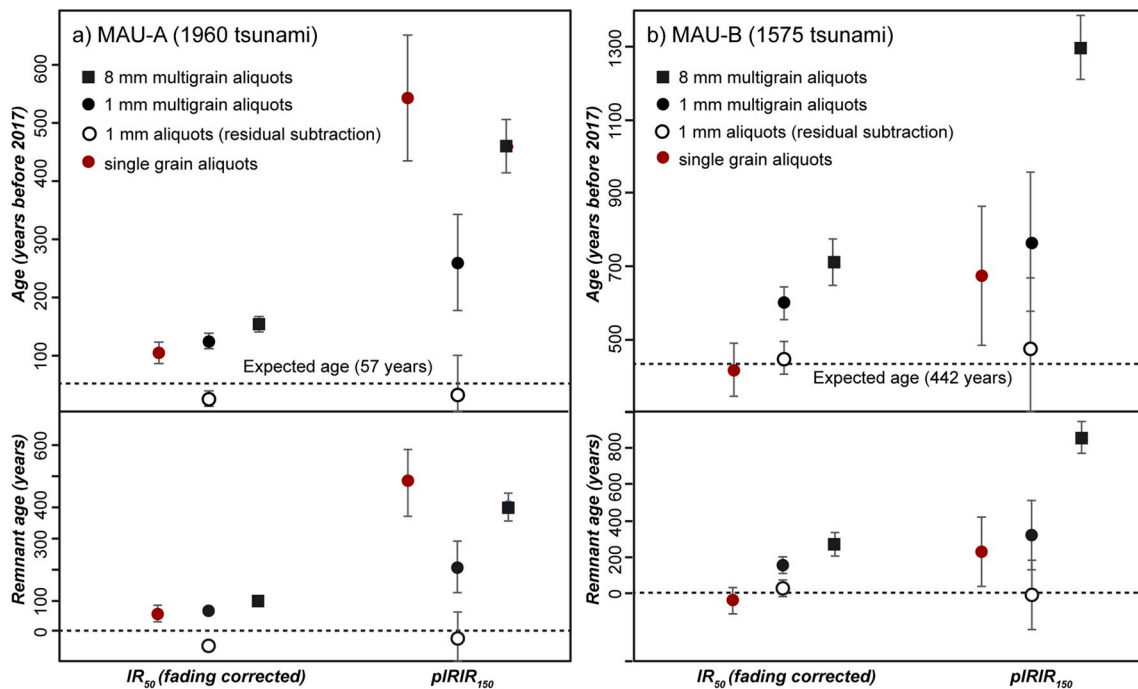

Fig. 8. Impact of aliquot size on OSL and remnant ages for sand sheets MAU-A (1960 tsunami) (a) and MAU-B (1575 tsunami) (b).

years to 40–750 years, no such effect is visible for the $pIRIR_{150}$ age of the same sample, likely due to its very dim signals (Fig. 8a). Despite this, single grains analyzed with the MAM_{bs} tend to provide ages in close agreement with control ages within their 1-σ confidence intervals for both the $pIRIR_{150}$ and the IR_{50} signal.

5. Discussion

5.1. Complement of the Chuyaquen seismic record

The Chuyaquen marsh had produced the first continuous paleoseismic record of the predecessors of the giant 1960 Chile earthquake (Cisternas et al., 2005). This radiocarbon-based chronology has been subsequently, and fruitfully, proven by different paleoseismic proxies (Atwater et al., 2013; Ely et al., 2014; Moernaut et al., 2014, 2018; Kempf et al., 2017; Garrett et al., 2015; Cisternas et al., 2018). However, the Chuyaquen chronology failed to date two of its recorded events, namely E and G. The present study solves this problem, offering luminescence ages for event E and radiocarbon and luminescence ages for event G. Thus, this two-millennia-long sequence is now much better constrained.

5.2. Stability of luminescence signals

The quartz ages of all Chuyaquen deposits older than 350 years systematically underestimate the control ages (Fig. 7a). Although not evidenced by falling D_e(time) plots (Fig. 5e), underestimation by thousand years, as observed for some samples, must be the result of an unstable quartz OSL signal. Pulse annealing experiments support the conclusion of thermally unstable net OSL signals (Fig. 5d), most likely arising from an unstable medium component that is dominating the net OSL signal even after early background subtraction. Unstable Chilean quartz signals, which equally affected tsunami and tidal deposits at Chuyaquen, were already reported in other studies (e.g. Steffen et al., 2009). An alternative to date such unstable quartz is by isolating a stable OSL fast component, as it was successfully performed for deposits of the 869 Jōgan tsunami in Japan (Tamura et al., 2015). However, due to the low sensitivity of the OSL signal in the Chuyaquen quartz, a robust extraction of its fast component was not possible. While there are also successful examples of quartz OSL dating from glacial and fluvial deposits with Pleistocene ages from Southern Chile (e.g. Duller, 2006; Rehak et al., 2010), unstable and insensitive OSL signals seem to make quartz from the studied sand layers unsuitable for luminescence dating. These differences might be linked to the age of the sediments or the lithology of their source areas. Although we did not carry out mineralogic studies to determine the source of the Chuyaquen sands, sediment starvation of the Maullín river, as sourced in a 300-m deep lake, and predominant wind, wave, littoral drift, and tidal current directions suggest that sediment coming from the Andes south of Maullín (roughly between 41° and 43° southern latitude) is the most likely sediment source.

Although less significant than in case of quartz, the IR_{50} feldspar ages of sands older than 350 years also underestimate the control ages (Fig. 7b). The obtained IR_{50} ages were corrected for fading using sample-specific g-values, but this approach was insufficient to correct for the complete signal loss during burial. The hypothesis of signal instability is supported by a trend towards increasing age underestimation with deposition age. The need for larger g-values to guarantee adequate fading correction is furthermore reinforced by results from nearby lake Huelde (Messens, 2014). There, obtained IR_{50} ages where assumed as accurate by using much larger g-values of 6–7%/decade. If similar g-values of 6.5%/decade are used for fading correction at Chuyaquen, good agreement with control ages is also achieved (Fig. 7b).

For sediments older than 350 years, the instability of both the quartz and the IR_{50} signals must even over-compensate any age overestimation due to thermally transferred residual signals and incomplete signal resetting as found for the two youngest tsunami sand sheets (this will be discussed in section 5.3). Although the effect of signal instability is less severe than for quartz OSL ages, IR_{50} ages corrected for fading using measured g-values still result in inaccurate chronologies for the tsunami and tidal deposits from Chuyaquen.

The best results in this study were obtained by $pIRIR_{150}$ dating of feldspar. Although the $pIRIR_{150}$ age of sand sheet E is still underestimated with significance on the 1-σ level, a systematic trend is not observed for this signal (Fig. 7c). While the ages of the two historical tsunamis are significantly overestimated, the majority of the older ages is in agreement with their control ages within their error margins. Subtraction of residual doses increases the number of $pIRIR_{150}$ ages that underestimate the control ages, but this is probably due to the large uncertainties introduced by correcting such young samples for relatively large residuals as reported by Reimann and Tsukamoto (2012). Even without fading correction the $pIRIR_{150}$ signal is, thus, considered the only luminescence signal used in this study with an adequate signal stability.

5.3. Resetting of luminescence signals

Over-dispersion and discrepancies between the CAM and MAM$_{bs}$

derived burial doses indicate incomplete luminescence signal resetting of all signals during sediment transport for most of the sand sheets. While partial bleaching was successfully addressed for samples older than 350 years by using the MAM$_{bs}$, the ages of the two younger tsunami sand sheets from 1960 and 1575 were still overestimated by the multigrain aliquot data of all three luminescence signals (Fig. 7). Both samples showed mean multigrain remnant ages of 60–180 years, for quartz OSL, 70–160 years, for IR_{50}, and 200–300 years, for $pIRIR_{150}$. Intriguingly, the 1960 tsunami deposit was previously dated much more accurately using large aliquots of quartz at Tirúa (Fig. 1b), an estuary located 360 km north of Chuyaquen (remnant ages of 10–30 years; Nentwig et al., 2015), and at Chuyaquen itself (less than 15 years; Eipert, 2004). However, age overestimation with remnant ages of several decades to a few centuries has been consistently reported elsewhere for tsunami deposits measured on large aliquots (Cunha et al., 2010).

The age overestimation for our samples could be explained in full by the observed laboratory residual doses of feldspar and by thermal transfer in quartz measurements. However, while the subtraction of residual doses successfully minimized age overestimation for the two youngest samples, it introduced significant age underestimation for some older ones (MAU-C1, MAU-D, MAU-E) (Fig. 7c). Partly, this may be due to general problems with correcting young samples for comparatively large residuals (Reimann and Tsukamoto, 2012), since the $pIRIR$ dating accuracy for young sediments is much better in settings with insignificant residuals (e.g. Madsen et al., 2011; Brill et al., 2018). However, in addition to that, influence of incomplete signal resetting is indicated by the fact that $pIRIR_{150}$ and IR_{50} remnant ages decrease with aliquot size (Fig. 8). Averaged signals from completely and incompletely bleached grains produce remnant ages of several decades to a few centuries when using multi-grain aliquots. On the contrary, when isolating the luminescence signals of the best-bleached grains using single-grain measurements a much lesser age overestimation was achieved.

Due to different transport modes and sediment sources of tsunami and tidal deposits, partial bleaching might also be reduced by dating tidal deposits instead of tsunami sand sheets. Tsunami deposits usually contain a mixture of well-bleached grains from the beach and incompletely bleached grains from subtidal or supratidal sediments (Brill et al., 2018). On the contrary, tidal deposits typically show a much more homogeneous bleaching (Madsen et al., 2005). Although differences between the $pIRIR_{150}$ ages of tsunami sand sheets (tendency to overestimation) and tidal deposits (in agreement with control ages or slight underestimation) observed in this study could just reflect different absolute ages (three of the four youngest sand sheets are tsunami layers), multigrain $pIRIR_{150}$ ages of tidal deposits generally tend to be less affected by incomplete bleaching than tsunami sand sheets.

In summary, remnant ages due to incomplete bleaching and laboratory residuals are large compared to the time since deposition in case of the two younger events at Chuyaquen, making $pIRIR_{150}$ dating rather inaccurate. However, remnant ages become less significant for older sand sheets. In case of quartz and IR_{50} ages, potential incomplete bleaching and effects of residual doses of sand sheets older than 350 years are masked by signal instability. But $pIRIR_{150}$ ages are not affected by significant instability and show reliable results for the older sand layers. While slight dating inaccuracies due to incomplete bleaching and residual doses must still be expected for $pIRIR_{150}$ ages of tsunami deposits up to ~2000 years, remnant ages of a few centuries will become insignificant for much older deposits.

5.4. Temporal and spatial variations of gamma and cosmic radiation

The results from Chuyaquen suggest that the selection of the appropriate luminescence signal for dating is the main aspect to be considered to avoid severe age over- or underestimation for both tsunami and tidal deposits. In comparison with this factor, the effect of time-dependent and spatially heterogeneous gamma and cosmic dose rates seems comparably insignificant, at least for sediments younger

than 2000 years. Standard procedures for dose rate determination that ignore these latter variations will produce only small inaccuracies, well within the 1-σ dating uncertainties.

6. Conclusions

While the influence of complex spatial and time-dependent dose rate patterns on luminescence dating accuracy is not significant within 1-σ dating uncertainties, appropriate consideration of signal stability and signal resetting are crucial for reliable luminescence chronologies in the investigated setting. Comparison with control ages, constrained by historical records and radiocarbon dates, shows that quartz and feldspar infrared ages corrected for fading using measured g-values systematically underestimate the age of deposition. Although this behavior is known for quartz from tectonically active regions, the signal instability additionally produced inaccurate infrared-stimulated feldspar ages, likely because fading correction was not sufficient.

While pulse annealing experiments might be indicative for quartz signal instability, the inadequate behavior for dating is not shown by other luminescence properties such as dose recovery, preheat-plateau tests or D_e(time) plots. In the end, signal instability for both quartz and feldspar is only unambiguously recognizable against control ages. Then, when working in regions with active orogeny, such as Chile, careful crosscheck with robust control ages is crucial to avoid systematic age underestimation, because stability won't be necessarily shown by the luminescence properties.

At Chuyaquen, only low-temperature post-infrared-stimulated feldspar signals (pIRIR$_{150}$) lack any systematic trend of age underestimation and are, therefore, interpreted to be stable at least on late Holocene timescales. Like in the cases of quartz and infrared-stimulated feldspar, a combination of laboratory residuals and incomplete signal resetting caused age overestimation of young tsunami deposits when pIRIR$_{150}$ was measured on multigrain aliquots. While these dating inaccuracies can be reduced by using single grain dating, in our study remnant ages remained problematic for pIRIR$_{150}$ when dating sand layers younger than a few centuries.

In sum, we conclude that paleoseismic events that took place in the last two millennia may be dated accurately with the pIRIR$_{150}$ signal of feldspar. This is particularly the case when their burial doses are based on single grain measurements, and when using tidal in favor of tsunami deposits. When dating older tsunami deposits, incomplete resetting and residual doses could be assumed to be less significant, allowing for using multigrain aliquots without significant dating inaccuracies.

Declaration of competing interest

The authors declare that they have no known competing financial interests or personal relationships that could have appeared to influence the work reported in this paper.

Acknowledgements

Appendix A. Supplementary data

Supplementary data to this article can be found online at https://doi.org/10.1016/j.quageo.2020.101080.

References

Angermann, D., Klotz, J., Reigber, C., 1999. Space-geodetic estimation of the Nazca-south America Euler vector. Earth Planet Sci. Lett. 171 (3), 329–334.

Atwater, B.F., Hemphill-Haley, E., 1997. Recurrence Intervals for Great Earthquakes of the Past 3.500 Years at Northeastern Willapa Bay, vol. 1576. U.S. Geological Survey Professional Paper, Washington, p. 108.

Atwater, B.F., Cisternas, M., Yulianto, E., Prendergast, A.L., Jankaew, K., Eipert, A.A., Fernando, W.I.S., Tejakusuma, I., Schiappacasse, I., Sawai, Y., 2013. The 1960 tsunami on beach-ridge plains near Maullin, Chile: landward descent, renewed breaches, aggraded fans, multiple predecessors. Andean Geol. 40 (3), 393–418.

Banerjee, D., Murray, A.S., Foster, I.D.L., 2001. Scilly Isles, UK: optical dating of a possible tsunami deposit from the 1755 Lisbon earthquake. Quat. Sci. Rev. 20 (5–9), 715–718.

Barrientos, S.E., 2007. Earthquakes in Chile. –. In: Moreno, T., Gibbons, W. (Eds.), The Geology of Chile, 263 – 288. Geol. Soc., London.

Bourgeois, J., 2009. Geologic effects and records of tsunamis. In: Bernard, E.N., Robinson, A.R. (Eds.), Tsunamis, vol. 15. Harvard University Press, Cambridge, Massachusetts, pp. 53–91.

Brill, D., Klasen, N., Jankaew, K., Brückner, H., Kelletat, D., Scheffers, A., Scheffers, S., 2012a. Local inundation distances and regional tsunami recurrence in the Indian Ocean inferred from luminescence dating of sandy deposits in Thailand. Nat. Hazards Earth Syst. Sci. 12 (7), 2177–2192.

Brill, D., Klasen, N., Brückner, H., Jankaew, K., Scheffers, A., Kelletat, D., Scheffers, S., 2012b. OSL dating of tsunami deposits from Phra Thong Island, Thailand. Quat. Geochronol. 10, 224–229.

Brill, D., May, S.M., Shah-Hosseini, M., Rufer, D., Schmidt, C., Engel, M., 2017. Luminescence dating of cyclone-induced washover fans at Point Lefroy (NW Australia). Quat. Geochronol. 41, 134–150.

Brill, D., Reimann, T., Wallinga, J., May, S.M., Engel, M., Riedesel, S., Brückner, H., 2018. Testing the accuracy of feldspar single grains to date late Holocene cyclone and tsunami deposits. Quat. Geochronol. 48, 91–103.

Buylaert, J.P., Jain, M., Murray, A.S., Thomsen, K.J., Thiel, C., Sohbati, R., 2012. A robust feldspar luminescence dating method for Middle and Late Pleistocene sediments. Boreas 41 (3), 435–451.

Chamberlain, E.L., Goodbred, S.L., Hale, R., Steckler, M.S., Wallinga, J., Wilson, C., (in press). Integrating geochronologic and instrumental approaches across the Bengal Basin: Earth Surface Processes and Landforms, https://doi.org/10.1002/esp.4687.

Cifuentes, I., 1989. The 1960 Chilean earthquakes. J. Geophys. Res. 94, 665–680.

Cisternas, M., Atwater, B.F., Torrejon, F., Sawai, Y., Machuca, G., Lagos, M., Eipert, A., Youlton, C., Salgado, I., Kamataki, T., Shishikura, M., Rajendran, C.P., Malik, J.K., Rizal, Y., Husni, M., 2005. Predecessors of the giant 1960 Chile earthquake. Nature 437 (7057), 404–407.

Cisternas, M., Carvajal, M., Wesson, R., Ely, L.L., Gorigoitia, N., 2017. Exploring the historical earthquakes preceding the giant 1960 Chile earthquake in a time-dependent seismogenic zone. Bull. Seismol. Soc. Am. 107 (6), 2664–2675.

Cisternas, M., Garrett, E., Wesson, R., Dura, T., Ely, L.L., 2018. Unusual geologic evidence of coeval seismic shaking and tsunamis shows variability in earthquake size and recurrence in the area of the giant 1960 Chile earthquake. Mar. Geol. 385, 101–113.

Cunha, P.P., Buylaert, J.P., Murray, A.S., Andrade, C., Freitas, M.C., Fatela, F., Munhá, J.M., Martins, J.A., Sugisaki, S., 2010. Optical dating of clastic deposits generated by an extreme marine coastal flood: the 1755 tsunami deposits in the Algarve (Portugal). Quat. Geochronol. 5 (2–3), 329–335.

Cunningham, A.C., Wallinga, J., 2010. Selection of integration time intervals for quartz OSL decay curves. Quat. Geochronol. 5 (6), 657–666.

Cunningham, A.C., Wallinga, J., 2012. Realizing the potential of fluvial archives using robust OSL chronologies. Quat. Geochronol. 12, 98–106.

del Rio, I., Sawakuchi, A.O., Gonzalez, G., 2019. Luminescence dating of sediments from central Atacama Desert, northern Chile. Quat. Geochronol. 53 https://doi.org/10.1016/j.quageo.2019.05.001.

Duller, G.A.T., 2006. Single grain optical dating of glacigenic deposits. Quat. Geochronol. 1 (4), 296–304.

Durcan, J.A., King, G.E., Duller, G.A.T., 2015. DRAC: dose rate and age calculator for trapped charge dating. Quat. Geochronol. 28, 54–61.

Eipert, A., 2004. Optically Stimulated Luminescence (OSL) Dating of Sand Deposited by the 1960 Tsunami in South-Central Chile (MSc, Carleton College).

Ely, L., Cisternas, M., Wesson, R., Dura, T., 2014. Five centuries of tsunamis and land-level changes in the overlapping rupture area of the 1960 and 2010 Chilean earthquakes. Geology 42 (11), 995–998.

Fan, A., Li, S.H., Li, B., 2011. Observation of unstable fast component in OSL in quartz. Radiat. Meas. 46, 21–28. https://doi.org/10.1016/j.radmeas.2010.10.001.

Galbraith, R.F., Roberts, R.G., Laslett, G.M., Yoshida, H., Olley, J.M., 1999. Optical dating of single and multiple grains of quartz from Jinmium rock shelter, northern Australia: Part I, experimental design and statistical models. Archaeometry 41, 339–364.

Garrett, E., Shennan, I., Woodroffe, S.A., Cisternas, M., Hocking, E.P., Gulliver, P., 2015. Reconstructing paleoseismic deformation, 2: 1000 years of great earthquakes at Chucalen, south central Chile. Quat. Sci. Rev. 113, 112–122.

Hogg, A., Hua, Q., Blackwell, P., Niu, M., Buck, C., Guilderson, T., Heaton, T., Palmer, J., Reimer, P., Reimer, R., Turney, C., Zimmerman, S., 2013. SHCal13 southern hemisphere calibration, 0–50,000 Years cal BP. Radiocarbon 55, 1889–1903.

Huntley, D., Baril, M., 1997. The K content of the K-feldspars being measured in optical dating or in thermoluminescence dating. Ancient TL 15 (1), 11–13.

Huntley, D.J., Lamothe, M., 2001. Ubiquity of anomalous fading in K-feldspars and the measurement and correction for it in optical dating. Can. J. Earth Sci. 38 (7), 1093–1106.

Kanamori, H., Cipar, J.J., 1974. Focal process of the great Chilean earthquake May 22, 1960. Phys. Earth Planet. In. 9, 128–136.

Kempf, P., Moernaut, J., Van Daele, M., Vandoorne, W., Pino, M., Urrutia, R., De Batist, M., 2017. Coastal lake sediments reveal 5500 years of tsunami history in south central Chile. Quat. Sci. Rev. 161, 99–116.

Kreutzer, S., Schmidt, C., DeWitt, R., Fuchs, M., 2014. The a-value of polymineral fine grain samples measured with the post-IR IRSL protocol. Radiat. Meas. 69, 18–29.

Lander, J.F., Lockridge, P.A., 1989. United States Tsunamis 1690-1988, vols. 41–2. National Geophysical Data Center Publ., Boulder, Colorado.

Lomnitz, C., 2004. Major earthquakes of Chile: a historical survey, 1535-1960. Seismol Res. Lett. 75 (3), 368–378.

Madsen, A.T., Murray, A.S., Andersen, T.J., Pejrup, M., Breuning-Madsen, H., 2005. Optically stimulated luminescence dating of young estuarine sediments: a comparison with 210Pb and 137Cs dating. Mar. Geol. 214 (1–3), 251–268.

Madsen, A.T., Buylaert, J.P., Murray, A.S., 2011. Luminescence dating of young coastal deposits from New Zealand using feldspar. Geochronometria 38, 379–390.

Messens, F., 2014. Luminescence Dating of Tsunami Sand in South Central Chile - a Feasibility Study (MSc, Universiteit Gent).

Moernaut, J., Van Daele, M., Fontijn, K., Heirman, K., Kempf, P., Pino, M., Valdebenito, G., Urrutia, R., Strasser, M., De Batist, M., 2018. Larger earthquakes recur more periodically: new insights in the megathrust earthquake cycle from lacustrine turbidite records in south-central Chile. Earth Planet Sci. Lett. 481, 9–19.

Moernaut, J., Van Daele, M., Strasser, M., Clare, M.A., Heirman, K., Viel, M., Cardenas, J., Kilian, R., Ladrón de Guevara, B., Pino, M., Urrutia, R., De Batist, M., 2017. Lacustrine turbidites produced by surficial slope sediment remobilization: a mechanism for continuous and sensitive turbidite paleoseismic records. Mar. Geol. 384, 159–176.

Moernaut, J., Van Daele, M., Heirman, K., Fontijn, K., Strasser, M., Pino, M., Urrutia, R., De Batist, M., 2014. Lacustrine turbidites as a tool for quantitative earthquake reconstruction: new evidence for a variable rupture mode in south central Chile. J. Geophys. Res. Solid Earth 119 (3), 1607–1633.

Murray, A.S., Wintle, A.G., 2003. The single aliquot regenerative dose protocol: potential for improvements in reliability. Radiat. Meas. 37 (4–5), 377–381.

Nentwig, V., Tsukamoto, S., Frechen, M., Bahlburg, H., 2015. Reconstructing the tsunami record in Tirúa, Central Chile beyond the historical record with quartz-based SAR-OSL. Quat. Geochronol. 30, 299–305.

Olley, J.M., Murray, A.S., Roberts, R.G., 1996. The effects of disequilibria in the uranium and thorium decay chains on burial dose rates in fluvial sediments. Quat. Sci. Rev. 15 (7), 751–760.

Plafker, G., Savage, J., 1970. Mechanisms of Chilean earthquakes of may 21 and may 22, 1960. Geol. Soc. Am. Bull. 81, 1001–1030.

Rehak, K., Niedermann, S., Preusser, F., Strecker, M.R., Echtler, H.P., 2010. Late Pleistocene landscape evolution in south-central Chile constrained by luminescence and stable cosmogenic nuclide dating. Geol. Soc. Am. Bull. 122 (7–8), 1235–1247.

Reimann, T., Tsukamoto, S., 2012. Dating the recent past (<500 years) by post-IR IRSL feldspar – examples from the north sea and baltic sea coast. Quat. Geochronol. 10, 180–187.

Riedesel, S., Brill, D., Roberts, H.M., Duller, G.A.T., Garrett, E., Zander, A., King, G.E., Tamura, T., Burow, C., Cunningham, A., Seeliger, M., De Batis, M., Heyvaert, V., Fujiwara, O., Brückner, H., Team, Q., 2018. Single-grain feldspar luminescence chronology of historical extreme wave event deposits recorded in a coastal lowland, Pacific coast of central Japan. Quat. Geochronol. 45, 37–49.

Riedesel, S., Autzen, M., Burow, C., 2019. scale_GammaDose( ): calculate the gamma dose deposited within a sample taking layer-to-layer variations in radioactivity into account (according to Aitken, 1985). Function version 0.1.1. In: Kreutzer, S., Burow, C., Dietze, M., Fuchs, M.C., Schmidt, C., Fischer, M., Friedrich, J. (Eds.), 2019. Luminescence: Comprehensive Luminescence Dating Data Analysis. R package version 0.9.0.87. https://CRAN.R-project.org/package=Luminescence.

Satake, K., Atwater, B., 2007. Long-term perspectives on giant earthquakes and tsunamis at subduction zones. Annu. Rev. Earth Planet Sci. 35 (1), 349–374.

Sherrod, B., 2001. Evidence for earthquake-induced subsidence about 1100 yr ago in coastal marshes of southern Puget Sound, Washington. GSA Bulletin 113 (10), 1299–1311.

Sievers, H., 1963. The seismic sea wave of 22 May 1960 along the Chilean coast. Bull. Seismol. Soc. Am. 53 (6), 1125–1190.

Spooner, N.A., 1994. The anomalous fading of infrared-stimulated luminescence from feldspars. Radiat. Meas. 23, 625–632.

Steffen, D., Preusser, F., Schlunegger, F., 2009. OSL quartz age underestimation due to unstable signal components. Quat. Geochronol. 4 (5), 353–362.

Tamura, T., Sawai, Y., Ito, K., 2015. OSL dating of the AD 869 Jogan tsunami deposit, northeastern Japan. Quat. Geochronol. 30, 294–298.

Thomsen, K.J., Murray, A.S., Jain, M., Botter-Jensen, L., 2008. Laboratory fading rates of various luminescence signals from feldspar-rich sediment extracts. Radiat. Meas. 43, 1474–1486.

Watanabe, H., 1998. Comprehensive List of Destructive Tsunamis to Hit the Japanese Islands. Univ. Tokyo Press, Tokyo ([in Japanese]).

Zander, A., Degering, D., Preusser, F., Kasper, H.U., Brückner, H., 2007. Optically stimulated luminescence dating of sublittoral and intertidal sediments from Dubai, UAE: radioactive disequilibria in the uranium decay series. Quat. Geochronol. 2 (1–4), 123–128.